A platinum nanowire electrocatalyst on single-walled carbon nanotubes to drive hydrogen evolution

T. Rajala, R. Kronberg, R. Backhouse, M.E.M. Buan, M. Tripathi, A. Zitolo, H. Jiang, K. Laasonen, T. Susi, Frederic Jaouen, et al.

Applied Catalysis B: Environmental 265 (2020) 118582

Contents lists available at ScienceDirect

Applied Catalysis B: Environmental

journal homepage: www.elsevier.com/locate/apcatb

A platinum nanowire electrocatalyst on single-walled carbon nanotubes to drive hydrogen evolution

T. Rajala[a], R. Kronberg[a], R. Backhouse[b], M.E.M. Buan[a], M. Tripathi[c], A. Zitolo[d], H. Jiang[e], K. Laasonen[a], T. Susi[c], F. Jaouen[f], T. Kallio[a,*]

[a] Department of Chemistry and Materials Science, Aalto University School Chemical Engineering, P.O. Box 16100, FI-00076 AALTO, Finland
[b] ITM Power, 22 Atlas Way, Sheffield, South Yorkshire S4 7QQ, United Kingdom
[c] University of Vienna, Faculty of Physics, Boltzmanngasse 5, A-1090 Vienna, Austria
[d] Synchrotron SOLEIL, L'orme des Merisiers, BP 48 Saint Aubin, 91192 Gif-sur-Yvette, France
[e] Department of Applied Physics, Aalto University School of Science, P.O. Box 15100, FI-00076 Aalto, Finland
[f] Institut Charles Gerhardt Montpellier, UMR 5253, CNRS - Université Montpellier - ENSCM, 2 place Eugène Bataillon, 34090 Montpellier, France

ARTICLE INFO

Keywords:
Hydrogen evolution
Ultralow Pt
Pt nanowire
Carbon nanotube

ABSTRACT

Pertinent existing hydrogen technologies for energy storage require unsustainable amounts of scarce platinum group metals. Here, an electrocatalyst comprising high-aspect-ratio platinum nanowires (PtNWs) on single-walled carbon nanotubes (SWNTs) with ultralow Pt content (340 $ng_{Pt}\,cm^{-2}$) is employed for hydrogen evolution reaction (HER). A comparable activity (10 mA cm^{-2} at −18 mV vs. RHE) to that of state-of-the-art Pt/C (38,000 $ng_{Pt}\,cm^{-2}$) is reached in acidic aqueous electrolyte. This is attributed to favorable PtNW interaction with SWNTs and PtNW edge-sites which adsorb hydrogen optimally and aid at alleviating repulsive interactions. Moreover, the metallic nature of Pt, morphological effects and enhanced wetting contribute positively. The PtNW/SWNT relevance is emphasized at a proton-exchange-membrane electrolyzer generating stable voltage for more than 2000 h, successfully competing with the state-of-the-art reference but with one tenth of Pt mass loading. Overall, this work presents an unprecedently efficient HER catalyst and opens up avenues for PtNW/SWNT catalyzing other high-impact reactions.

1. Introduction

A major technological obstacle with the spread of solar and wind energy is its storage for cloudy and windless occasions. Power-to-gas energy storage *via* water electrolysis is one of the few options for storing excess renewable energy at large scales and over long time periods. In this process, electrical power is converted to chemical energy in the form of hydrogen. Hydrogen is an ideal energy carrier in the sense that it is abundant and has the highest gravimetric energy density among conventional fuels. [1] However, 90 % of the world's hydrogen is currently produced from fossil fuels with considerable CO_2 emissions, and therefore electrolysis of water attracts increasing interest as a sustainable alternative. [2–4]

The hydrogen evolution reaction (HER), $2H^+ + 2e^- \rightarrow H_2$, is one of the necessary half-reactions in water splitting. By storing energy in hydrogen by splitting water, the energy can subsequently be released back in a fuel cell, for instance to power electric vehicles and portable electronics. [5] Alternatively, the hydrogen energy carrier can be used in industrial processes such as chemical, fertilizer or steel production.

A barrier to large scale deployment of cutting edge polymer electrolyte membrane (PEM) electrolyzers is a strong dependence on rare and expensive platinum group metals (PGMs). Decreasing the amount of the PGMs is important for laying the groundwork for the large-scale and long-term deployment of H_2 fuel. This has driven research into non-noble metal alternatives such as transition metal phosphides [6,7], carbides [8] and nitrides [9,10] or chalcogenides [11–13]. For the time being, however, Pt-based HER catalysts are still regarded as the most relevant starting point owing to their better overall performance in activity, stability and integrability to industrial applications such as PEM electrolyzers in acidic environment [14,15].

As to PEM electrolyzers under acidic operating conditions, the cathode can suffer from high degradation. [16] On conventional carbon black substrates, Pt nanoclusters tend to agglomerate during operation with the on/off electrochemical cycles of an electrolyzer connected to a renewable energy source. This has hitherto led to an antagonism between ultralow Pt loadings (< 1000 $ng_{Pt}\,cm^{-2}$) (achievable only with

* Corresponding author.
E-mail address: tanja.kallio@aalto.fi (T. Kallio).

https://doi.org/10.1016/j.apcatb.2019.118582
Received 6 November 2019; Received in revised form 18 December 2019; Accepted 29 December 2019
Available online 30 December 2019

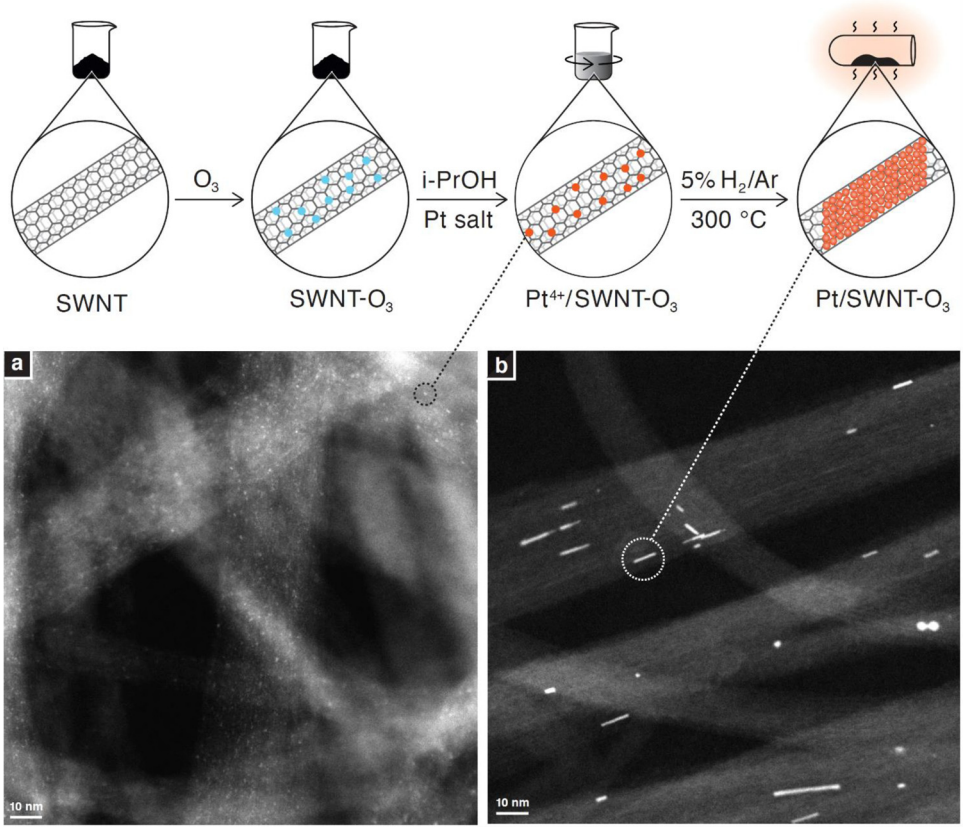

Fig. 1. Schematic illustration of the synthesis of Pt/SWNT-O_3 with Pt content of 3.9 wt%.. a. HAADF/STEM image of the CNT bundles with Pt/SWNT before the heat treatment. b. HAADF/STEM image of the CNT bundles with Pt nanowires after the heat treatment. The scale bars are 10 nm.

the highest Pt mass activity, i.e. nanometric Pt objects) on one hand and the high durability requirements of a PEM electrolyzer on the other.

In order to prevent the loss of active Pt *via e.g.* Ostwald ripening, Pt nanoparticle growth and detachment of Pt nanoparticles during catalysis, metal oxide supports with stronger interaction with Pt nanoparticles have been suggested. [17–22] However, their electronic conductivity is low and the oxides are prone to reduction under low HER potentials, rendering the support unstable. Promising ultralow-Pt supports for the HER have been reported based on conductive carbon materials such as N-doped graphene [23], $Ti_xW_{1-x}C$ [24], and carbon nanospheres [25] that do allow good activities and stabilities but still fall short of successful incorporation in an actual electrolyzer cell.

Carbon nanotubes, on the other hand, can assist in bringing together the ideals of high activity, stability and integrability as we show in this article. Especially single-walled carbon nanotubes (SWNTs) provide highly conductive and durable supports for accommodating even ultralow amounts of subnanometric Pt catalyst particles because of their unique morphology. [26] Now that the price of SWNTs has notably decreased in recent years due to the upscaling of their synthesis, their adoption for high-end electrocatalytic applications is favorable over multi-walled carbon nanotubes as has also been concluded elsewhere [27].

In this work, we aim to mitigate PGM dependency by presenting a simple and upscalable synthesis of Pt nanowires (PtNWs) on SWNTs. Our approach to improve the adhesion, and thus durability, of PtNWs on SWNT relies on controlled surface oxidation with ozone, whereas electrocatalytic activity and stability are attributed to morphological effects.

For an ozone-treated SWNT substrate [28] with 340 $ng_{Pt}\,cm^{-2}$ (Pt/SWNT-O_3), we report a HER activity of 10 mA cm^{-2} at $-18\,mV_{RHE}$, being competitive to a state-of-the-art Pt/C catalyst (38,000 $ng_{Pt}\,cm^{-2}$) that attains the same current density at $-16\,mV_{RHE}$ but with notably higher Pt mass loading. Equally ultralow and pseudo-atomic Pt on SWNT (570 $ng_{Pt}\,cm^{-2}$) has earlier been presented by Tavakkoli et al. [26] In contrast, Pt/SWNT-O_3 with similar Pt loading does not become deactivated under negative HER potentials as observed by Tavakkoli et al. The improved stability is attributed to interactions between the PtNWs and the SWNT support inducing compressive strain in the Pt bonds and resulting optimal hydrogen inaction with PtNWs.

The feasibility of our Pt/SWNT-O_3 catalyst is verified in a single-cell PEM electrolyzer. In terms of activity, even with one tenth of Pt mass loading at the cathode (0.02 $mg_{Pt}\,cm^{-2}$), Pt/SWNT-O_3 performs close to the level of the state-of-the-art Pt/C material. The stability and durability of Pt/SWNT-O_3 as a cathode catalyst are confirmed with more than 2000 h of chronopotentiometric measurements and 10,000 potential cycles simulating on/off operation.

We conclude that strain in the Pt bonds, the metallic nature of PtNWs and, with respect to the morphology, the PtNW edges in particular contribute positively to the overall performance. The clear catalytic enhancement achieved by the ozone treatment is attributed not only to morphological effects but also to improved hydrophilicity of the catalyst. Moreover, the simple synthesis of PtNW/SWNT presented in this study allows for both upscaling in volume and testing in industrially relevant applications.

2. Catalyst synthesis and characterization

First, the SWNTs (OCSiAl TUBALL™, diameter 2 nm, 90 wt% SWNT, 3 wt% metal impurity) were functionalized using an ozone generator (Enaly OZX-300ST). An ozone flow of 200 mg/h was directed over the pristine SWNTs for 40 min to increase their surface activity and hydrophilicity, thus assisting the transfer of Pt from $H_2PtCl_6 \cdot 6\,H_2O$ (Alfa Aesar) onto the SWNT surface.

As a reference, a material using pristine SWNTs and $H_2PtCl_6 \cdot 6\,H_2O$

was prepared. For this, the same synthesis process was used but omitting the ozonation step.

The pretreated or pristine SWNTs were dispersed in relation of 1 mg per 1 ml of i-PrOH (Fischer Scientific) by ultrasonication for 15 min. After this, while mixing by magnetic stirring, Pt was introduced by adding $H_2PtCl_6 \cdot 6\ H_2O$ in ethanol to obtain the desired concentration. This was again followed by ultrasonication for 15 min and magnetic stirring overnight.

Subsequently, the well-dispersed ink was gradually heated up to 300 °C in N_2 at a rate of 100 °C/h to first evaporate the solvent and counter ions. At 300 °C, N_2 was switched to 5 % H_2/Ar for 2 h to reduce the Pt(IV). The synthesis procedure is outlined in Fig. 1. After the heat treatment, the sample was cooled down to room temperature under an N_2 atmosphere and collected to begin with electrochemical experimentation as detailed in the Supporting Information (SI). The synthesis yield of the catalyst was ca. 88 %.

In addition to electrochemical experimentation, the material was thoroughly characterized with physical methods, including scanning transmission electron microscopy (STEM), inductively coupled plasma mass spectroscopy (ICP-MS), Raman spectroscopy, X-ray photoelectron spectroscopy (XPS), X-ray absorption spectroscopy (XAS) including extended X-ray absorption fine structure (EXAFS), and goniometry. Computational studies are included to shed light on the catalytic properties of the PtNW/SWNT structure. Further details about the experimental methods are discussed in the SI.

3. Results and discussion

3.1. The PtNW structure on the SWNTs

The highest electrochemical activity is attained when the SWNTs are treated with ozone, before adding the Pt complex. The method of oxidizing the carbon support before depositing metal catalysts has been previously reported. [28–32] In our synthesis, the ozone step introduces polar oxygen functional groups on the SWNT surface as revealed by XPS (see Fig. 8 and Table 2 in XPS section), improving the adhesion of the ionic Pt precursor.

Striking Pt nanowire structures are formed by heating the material in 5 % H_2/Ar atmosphere at 300 °C for two hours. Fig. 1a and b represent STEM images of the catalyst before and after the heat treatment and demonstrate the presence of sub-nanometer Pt clusters before the heat-treatment and appearance of PtNWs only after the heating step. In addition, some Pt still remains as small clusters observed as clear bright spots (Fig. 1b). Energy dispersive X-ray spectroscopy (EDS) measurements confirm that both the NWs and the subnanoparticles consist of Pt.

Based on our earlier observations, sub-nanometer Pt clusters are formed only on SWNTs [26], which is attributed to the curved nature of the SWNTs promoting asymmetric diffusion of the adsorbed Pt atoms: In axial direction diffusion is sluggish but in radial direction it is fast and this stabilizes sub-nm Pt cluster. These sub-nm Pt particles are needed to form PtNWs (see Fig. 1) during the heat-treatment procedure because larger spherical agglomerates are more stable and do not form such NW structures.

Interestingly, without the ozone modification of the SWNTs, the deposited PtNWs are longer (see Fig. 2). For Pt/SWNT and Pt/SWNT-O_3 with similar Pt contents of 3.2 wt% and 3.9 wt%, respectively (determined by ICP-MS), the average lengths of the PtNWs are 65.6 nm and 16.4 nm. The size distributions of the PtNWs on both SWNTs and ozonized SWNTs are obtained from high-magnification STEM images and depicted by histograms in Fig. 2. In terms of width, there is no significant difference between the two samples (Figure S1).

In both Pt/SWNT and Pt/SWNT-O_3, Pt appears crystalline even though no single lattice orientation can be distinguished (Fig. 2c and f). In addition to the nanowires, the high-resolution HAADF/STEM image in Fig. 2f also shows the presence of subnanometric Pt clusters and even individual Pt atoms which apparently form as a result of the ozone treatment of the SWNTs. Such tiny Pt clusters are expected to show a high initial catalytic activity, but become deactivated within a few minutes. [26]

3.2. Electrochemical activity of the catalysts

The HER activity of ozone-treated Pt/SWNT-O_3 is contrasted with its non-treated counterpart Pt/SWNT and a state-of-the-art Pt/C reference. The electrocatalytic benefit of pretreating the SWNTs with ozone before introducing Pt is clearly shown in Fig. 3. At a potential of $-0.05\ V_{RHE}$ in acidic electrolyte, 3.2 wt% Pt/SWNT and 3.9 wt% Pt/SWNT-O_3 generate current densities of 10 and 35 mA cm^{-2}, respectively, while the 20 wt% Pt/C reaches 40 mA cm^{-2}. Fig. 3b displays the HER (mass) activities of the catalysts normalized by their corresponding Pt loadings. Evidently, the ozonized Pt/SWNT-O_3 catalyst has the highest HER mass activity of the three. A literature comparison with other low-Pt and nanosized Pt cluster catalysts show the good performance of Pt/SWNT-O_3 and is presented in Supplementary Information (Table S1).

Fig. 3a also presents the HER polarization curves for a wt% series of the Pt/SWNT-O_3 catalyst along with the commercial 20 wt% Pt/C. The activity enhancement achieved by adding even a small amount of Pt on the SWNTs is evident when comparing the HER performance with pristine and ozone-treated SWNTs. The catalyst prepared from SWNT-O_3 with 3.9 wt% of Pt outperforms the other Pt/SWNT-O_3 catalysts with other Pt contents and almost coincides with the commercial reference. Besides, this Pt loading has the highest electrochemically active surface area (ECSA) (Table S2) among the experimented ones as discussed below. Therefore, the 3.9 wt% Pt/SWNT-O_3 catalyst is selected as the optimal candidate for further examination by electrochemical and physical characterization methods.

The ECSAs are determined from CO stripping experiments (Figure S10 and Table S2). The differences in the PtNW morphology and the structural changes of the SWNT support are reflected as a tripling of ECSA for Pt/SWNT-O_3 compared to Pt/SWNT. The decrease of ECSA with the increase in the Pt loading of the catalysts with ozone treated SWNT support may be attributed to formation of less active spherical agglomerates with a lower area-to-volume ratio. Interestingly, Pt/SWNT-O_3 with ultralow Pt loading shows an ECSA of 29 $m^2\ g_{Pt}^{-1}$ comparable to the ECSA of the commercial Pt/C (35 $m^2\ g_{Pt}^{-1}$) with a notably higher Pt loading. The HER activities of Fig. 3a normalized with ECSA are presented in Figure S2.

Local fluctuations in the linear trends of the HER curves of Fig. 3 are attributed to the vigorous evolution of H_2 bubbles. [33,34] IR-corrected polarization and Tafel curves are presented in Figures S3 and S4, respectively. Changes in the electrolyte resistance (measured by electrochemical impedance spectroscopy) from experiment-to-experiment are found negligible (Figure S5) and thus the same conclusions can be derived irrespective of the *iR* correction.

The shorter length of the nanowires on the ozonized SWNTs suggests one plausible cause behind the higher HER activity. As according to Fig. 3b, the difference in Pt content is not enough to account for the difference in activity, the higher number of active edges and corners for the shorter PtNWs are suggested to promote the HER (see computational results). Enhanced hydrophilicity, or wetting of the surface, as shown by goniometric studies (Figure S6), may also contribute to the facilitated HER by improving the mass transfer to the Pt/SWNT-O_3 electrocatalyst surface. [35,36]

Higher hydrophilicity of Pt/SWNT-O_3 compared to Pt/SWNT is attributed to surface structural changes induced by the ozone treatment. These include formation of functional groups with oxygen on the surface of the SWNTs according to XPS (Fig. 8 and Table 2) and carbon bonding of SWNTs as observed by Raman (Figure S7). Raman characterization revealed an increase in the amount of disorder carbon in comparison to graphitic sp^2 carbon network after the ozone treatment since there is a significant decrease of the I_G/I_D ratio from 56.7 to 3.3

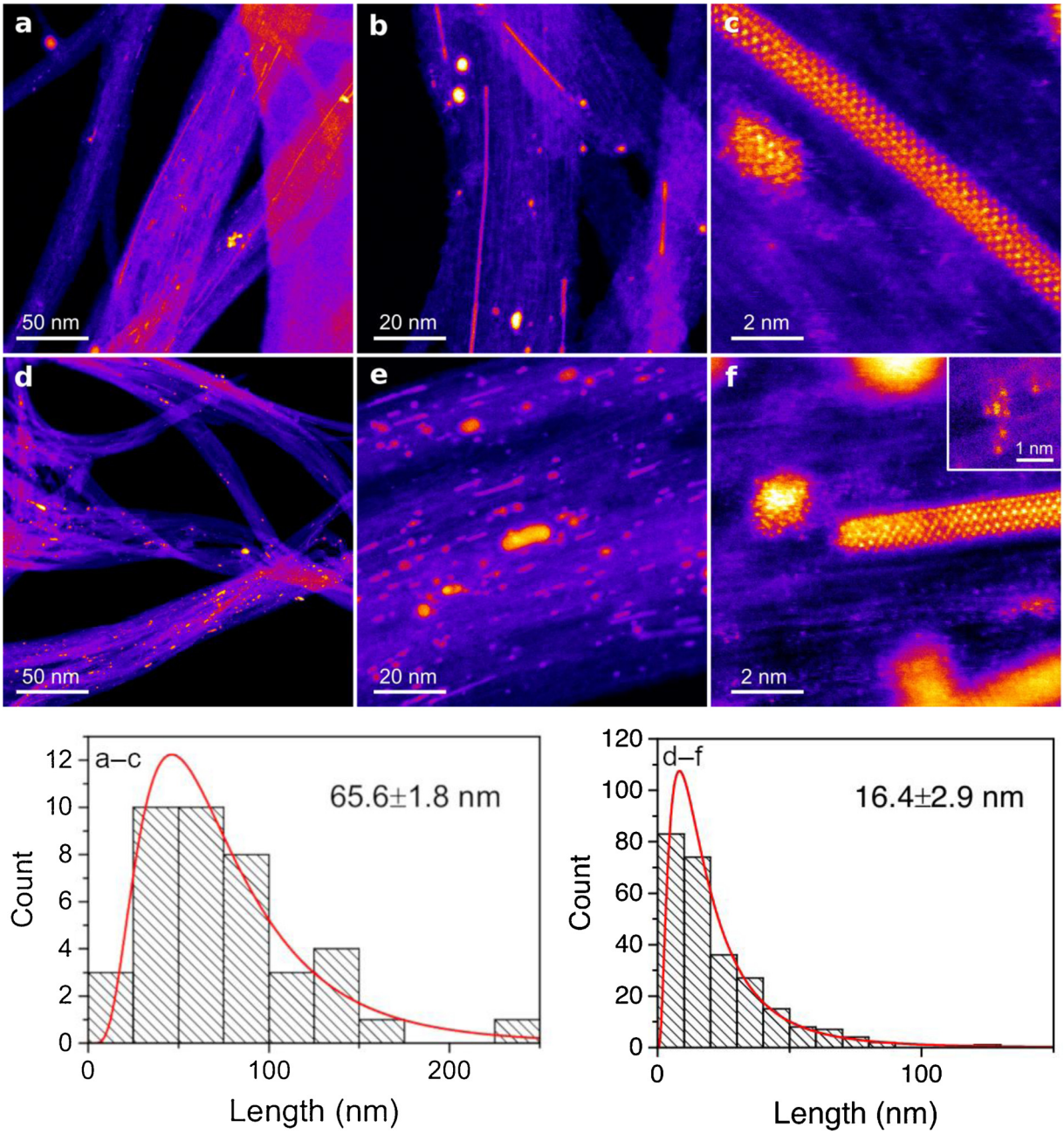

Fig. 2. Above: HAADF/STEM images (colored to enhance contrast) of Pt/SWNT (panels a–c) and of Pt/SWNT-O_3 (panels d–f) at different magnifications. The inset to panel f shows a closer view of several individual Pt atoms clustered loosely together. Below: The nanowire length distributions of 3.2 wt% Pt/SWNT (a–c) and 3.9 wt % Pt/SWNT-O_3 (d–f).

for the SWNTs. Here, I_G refers to the Raman intensity arising from graphitic sp^2 carbon whereas I_D is attributed to disordered carbon. Similar differences in the Raman spectra are also observed for Pt-SWNT and Pt-SWNT-O_3, indicating that the structural changes induced by the ozone treatment remain after the Pt deposition and the reduction step of the synthesis.

The structural differences induced by the ozone treatment on the SWNT support and Pt is also reflected as higher currents in the cyclic voltammograms (CVs in Figures S8 and S9), both for the Pt containing catalysts and for the SWNT supports. These differences induced by the ozone treatment are discussed in more detail below in Sctions 3.3. and 3.4 Furthermore, the CV of SWNT-O_3 is featured by a redox peak pair at the potential range of 0.4…0.8 V_{RHE}, which is absent in pristine SWNT and hence attributed to oxygen containing groups. What is noteworthy at CV potentials lower than ca. 0.3 V_{RHE}, is the absence of adsorption/desorption peaks in the hydrogen fingerprint region (Figure S8). The featureless CVs may simply result from the ultralow Pt loadings of 279 ng cm^{-2} for Pt/SWNT and 340 ng cm^{-2} for Pt/SWNT-O_3.

The stability of Pt/SWNT-O_3 is confirmed by an accelerated stress test (AST), consisting of 3400 CV cycles between −0.08 and 0.8 V_{RHE}. The upper limit corresponds to the potential reached for the cathode of an electrolyzer during a shut-down process because of its spontaneous polarization induced by remaining oxygen transferred from the anode to the cathode. [37] Fig. 4 demonstrates the HER activity of the 3.9 wt% Pt/SWNT-O_3 catalyst before and after the AST, where a negligible change in the activity indicates good durability. Throughout the potential range in which the formation of H_2 bubbles is moderate enough to maintain the curves linear and comparable, the potential loss is no more than 5 mV. Furthermore, in comparison to what has been earlier presented by Tavakkoli et al. [26] for equally ultralow Pt on SWNT

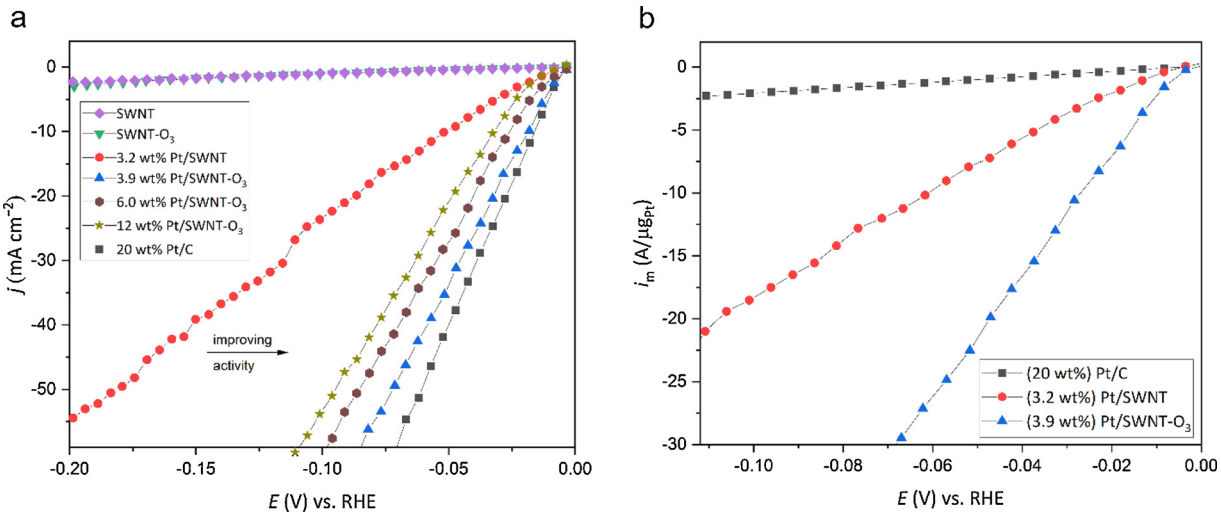

Fig. 3. HER polarization curves for Pt/SWNT catalysts with and without ozone treatment contrasted with commercial 20 wt% Pt/C from Alfa Aesar in H_2 saturated 0.5 M H_2SO_4. Catalyst loading 0.2 mg/cm^2, scan rate 2 mV/s, rotation speed 2500 rpm. Normalized with **a**. electrode area **b**. Pt mass.

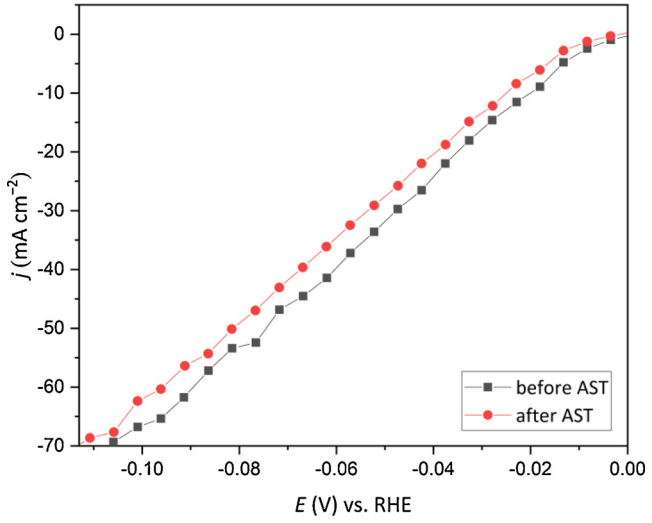

Fig. 4. HER polarization curves for Pt/SWNT-O3 before and after an accelerated stress test (AST). Scan rate 2 mV/s, rotation speed 2500 rpm.

(570 $ng_{Pt}\,cm^{-2}$) as here, Pt/SWNT-O_3 maintains its activity under negative HER potentials (Figure S11).

Fig. 5a presents the performance of Pt/SWNT-O_3 as the cathode catalyst of a PEM electrolyzer setup under acidic conditions. Pt/SWNT-O_3 has now a ten times lower Pt loading per electrode area than the commercial Pt/C reference. The onset voltages of the polarization curves are close to each other, suggesting similar intrinsic activity towards the pertinent electrochemistry. However, the novel Pt/SWNT-O_3 catalyst shows a higher operating voltage with increased current density compared to the standard Pt/C, which is probably related to differing resistances in the membrane electrode assembly. In the impedance spectra (see Figure S12) measured for the cell equipped with 0.02 $mg_{Pt}\,cm^{-2}$ of Pt/SWNT-O_3 an additional potential independent *RC* circuit appears when compared to spectra measured for the electrolysis cell with ten times higher loading of commercial Pt/C. This is attributed to the cathode processes becoming limiting because of the low Pt content and suggest that further reduction of Pt is not feasible due the increase of operation voltage. On the other hand, similar cell resistances obtained for both the set-ups suggest that the electronic conductivity of the ozone treated SWNTs is high enough for this application though ozone treatment is known to decrease conductivity of SWNTs [28].

When decreasing the Pt content of the commercial electrode to the level of Pt/SWNT-O_3, the polarization curves show similar activity (Figure S13a). However, the long-term voltage profile at a constant current density of 1 A cm^{-2} is better for the novel catalyst most likely due to improved mass transfer (Figure S13b). This is attributed to dissimilar surface properties and morphologies of the electrocatalysts plausibly resulting in divergent interactions between the catalyst and the ionomer and the species participating the reactions.

The stability of the electrolyzer setup with Pt/SWNT-O_3 at the cathode is tested by operating the cell at the constant current density of 1 A cm^{-2} for 2,000 h (Fig. 5b). The MEA with this catalyst shows stable performance with a small voltage drop after 320 h since the contact is enhanced by inserting a GDL in place at the cathode.

The stability is also investigated with an AST where the cathode catalyst is sprayed onto a carbon paper with a Nafion content of 30 wt %. This membrane is transferred into a test cell with in-situ reference electrode to carry out the AST to investigate changes in the ECSA as a result of power cycling. It has been shown that when the electrolyzer is switched off, the cathode contributes more to changes at OCV than the anode. [16] This can lead to various degradation processes such as Pt nanoparticle growth via migration and surface diffusion and Pt detachment or agglomeration due to carbon support corrosion induced by oxygen diffusion from the anode to the cathode during the shut-down phase. The change in ECSA with number of cycles is plotted in Fig. 5c. However, it should be noted that at the chosen catalyst loading, the changes in the ECSA do not have an impact on the overall cell voltage as the HER on Pt is such a facile reaction.

The general ECSA trends with on-going voltage cycling for the two materials are displayed in Fig. 5c and are in agreement with the values measured in the electrochemical cell taking into account the large error margins and different operation environments (aqueous acid electrolyte *vs.* PEM). The initial ECSA of 44 $m^2\,g_{Pt}^{-1}$ for the Pt/SWNT-O_3 is well in the range of the Pt/C reference. After 9000 potential cycles, the degradation results in 19 $m^2\,g^{-1}$ for the Pt/SWNT-O_3 while 21 $m^2\,g^{-1}$ for the Pt/C. Although our catalyst does not succeed quite as well as the reference, the end result of the ECSA test still suggests comparable endurance under oxidative shut-down cycles. Overall, the performance of the novel Pt/SWNT-O_3 catalyst approaches that of the standard Pt/C even though the Pt loading is only one tenth.

3.3. XAS/EXAFS analysis of catalysts

XAS analysis was carried out to investigate the overall structural features of PtNWs, which dominate the spectral response over the subnanometer particles and which can be linked with the observed

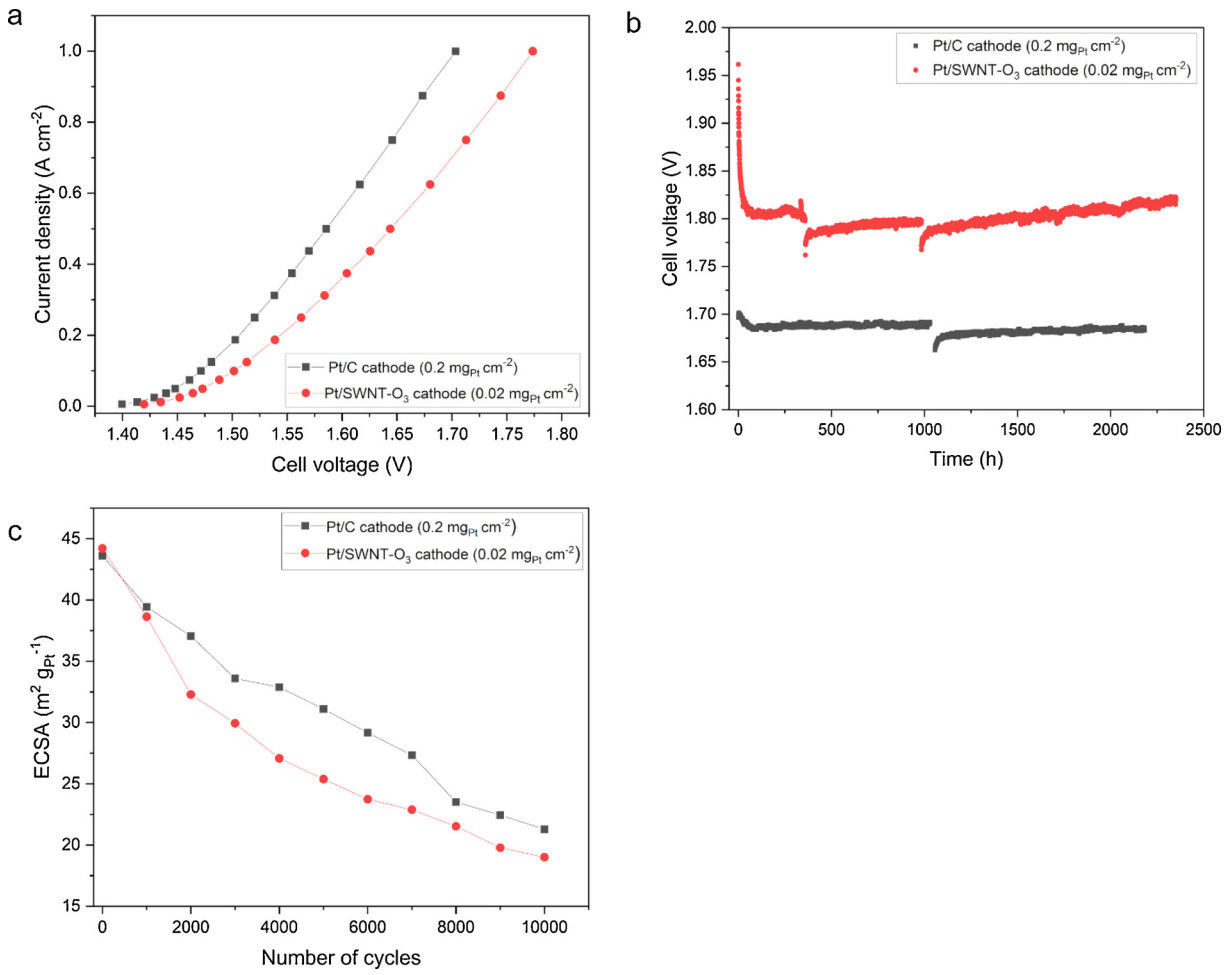

Fig. 5. Electrolyzer tests recorded at 55 °C using Nafion®-115 membrane and 0.2 mg cm^{-2} of Pt/C or 0.02 mg cm^{-2} of Pt/SWNT-O_3 at the cathode, while having 3 mg cm^{-2} of $IrRuO_x$ at the anode. **a**. Polarization curves and **b**. voltage profiles during constant current operation at 1 A cm^{-2} and **c.** Electrochemically active surface area recorded every 1000 cycles, normalized to Pt loading.

electrocatalytic activity. Figure S14 shows a comparison between the experimental Pt L_3-edge X-ray absorption spectra of the ozonized and non-ozonized Pt/SWNT samples and the reference Pt foil. There are no changes in the position of the threshold energy and in the frequency of the spectral oscillations, confirming the metallic nature of the PtNWs.

An in-depth EXAFS analysis of Pt/SWNT and Pt/SWNT-O_3 was carried out starting from a rigorous fit of the crystalline Pt used as a known reference structure, on the basis of which a comprehensive understanding of the local atomic structure in Pt nanosystems was achieved. The details of the fitting procedure are discussed in SI, while the best-fit analysis and the structural parameters obtained for each Pt sample are presented in Fig. 6 and Table 1.

As is shown in Fig. 6, the agreement between the experimental and calculated EXAFS spectra of the Pt foil is very good in the whole energy range, and the structural parameters (determined up to the fifth coordination shell) are, within the statistical errors, in perfect agreement with previous crystallographic determinations, [38] establishing the reliability of the data-analysis method. As far as Pt/SWNT and Pt/SWNT-O_3 are concerned, despite the low Pt content, the quality of the EXAFS signal is still very satisfactory, providing the possibility to investigate the structural features up to the fourth coordination shell. The most visible change between the spectra of crystalline Pt and PtNW/SWNTs is the reduction of the EXAFS signal in the nanocrystal systems. This effect became more apparent observing the Fourier transform of the EXAFS spectra depicted in Fig. 7, and more pronounced for the peaks in the region of 3.5–6 Å, corresponding to the higher coordination shells, that are the most affected by nanoscale effects. This damping is usually due to a decrease in the coordination number, yet the first shell coordination number is practically unaffected in two PtNW/SWNTs compared to Pt foil (see Table 1). This can be explained by the simultaneous increasing in the structural disorder in the order Pt/SWNT > Pt/SWNT-O_3 > Pt foil (quantified by the Debye Waller factor reported in Table 1), which is known to have an impact on the signal amplitude. Therefore, in both PtNW/SWNTs, the first shell signal reduction is mainly due to an increase in the structural disorder, while the higher shells are simultaneously affected by the rise of the structural disorder and a decrease in the coordination number. At the same time, our EXAFS results clearly show a contraction of the average Pt-Pt distances for PtNW/SWNTs relative to bulk Pt, with a larger reduction for the non-ozonized Pt sample (see Table 1). One possible explanation for this phenomenon is an increase in the surface strain as a consequence of the high curvature of the nanowires as is further discussed in the computational part. [39]

Compressive strain is known to downshift the d-band center of the late transition metals, thus weakening the interaction between the adsorbate and the surface. [40] Consequently, the HER current is enhanced by the observed compressive interaction between the support and Pt if hydrogen bonding is too strong. When comparing the HER current stability on Pt/SWNT-O_3 (Figure S11) to our earlier study on pseudo-atomic Pt on SWNT, [26] it is obvious that the latter suffers from current decay when subjected to the HER potential region. This phenomenon is attributed to contamination of the pseudo-atomic Pt surface by adsorbed hydrogen, resulting from too strong hydrogen

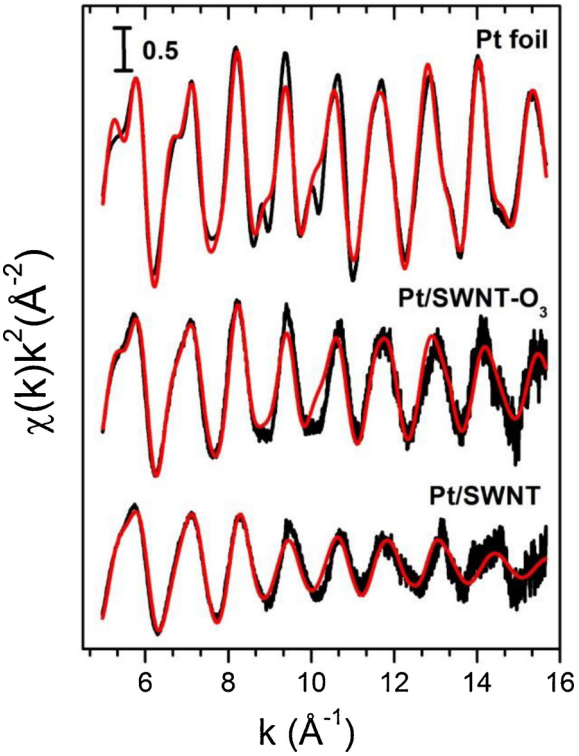

Fig. 6. Comparison between the best-fit theoretical signals (red lines) and the experimental EXAFS χ(k) signals (black lines) for Pt foil, Pt/SWNT-O3 and Pt/SWNT. χ(k) signals are shown multiplied by k2 for a better visualization. (For interpretation of the references to colour in this figure legend, the reader is referred to the web version of this article).

bonding. These observations suggest that the hydrogen bonding is closer to the optimal H−H bonding range for the PtNW morphology (see Table S3 for relative changes in Pt bond distances) and the observed current can be mainly attributed to these structures for Pt/SWNT-O_3, and not the individual Pt atom clusters also observed in STEM (see Fig. 2).

Table 1 emphasizes the variation of the most representative structural parameters of the PtNW/SWNT samples relative to bulk Pt (see also Table S3). It is important to note that in the case of PtNW/SWNTs, the accuracy related to the structural parameters decreases from the second coordination shell, the error bars depending on the greater noise level of the experimental EXAFS spectra compared to the data of the Pt foil.

3.4. XPS analysis of catalysts

The elemental composition of the samples was assessed using XPS. Measurements of the SWNTs before and after the ozone treatment showed that the pure SWNTs contained only 0.7 at% oxygen, while after ozone exposure the oxygen content increased to 2.9 at% (see Table 2).

When Pt was deposited on ozone functionalized SWNTs a higher amount of Pt is present on the surface compared to when Pt s deposited on pristine SWNTs. The Pt/SWNT sample contained 0.05 at% Pt (0.8 wt %), while for Pt/SWNT-O_3 the amount of Pt is double at 0.11 at% (1.7 wt%). These values are lower than the Pt content obtained using ICP-MS measurements, which may be due to XPS being a surface sensitive technique. As discussed above in connection to the XAS measurements, the Pt is mainly present as Pt° for both Pt/SWNT and Pt/SWNT-O_3 as can be observed from the asymmetric peak shape of the Pt 4*f* peaks (Fig. 8 a). Deconvolution of the Pt 4*f* peaks for both samples indicates the presence of 72 % metallic Pt (Pt° $4f_{7/2}$ at 71 eV), 18 % PtO (Pt^{2+} $4f_{7/2}$ at 72.3 ± 0.1 eV), and 10 % of oxides such as PtO_2 (Pt^{4+} $4f_{7/2}$ at 73.9 ± 0.1 eV). [41,42] Most of the Pt surface is thus reduced by the heat treatment at 300 °C in a 5 % H_2/Ar flow (Fig. 1). Even though the Pt 4f profiles are similar for the two samples, Pt/SWNT-O_3 contains twice as much metallic Pt and PtO_x as Pt/SWNT before performing HER.

All samples contain elements besides Pt, C and O, originating from the production process of the SWNTs such as Fe and S from the SWNT growth-catalyzing particles. The detected amount of Fe increases after Pt deposition, most likely due to the exposure of carbon-encapsulated Fe particles by the synthesis procedure. However, the presence of Fe particles does not influence the HER activity of the Pt/SWNT samples as the SWNTs alone do not exhibit any catalytic activity (Fig. 3a).

While ozone treatment increased the amount of oxygen functional groups in the surface of the SWNTs, the synthesis procedure for Pt deposition also introduced significant amounts of oxygen. While the pure SWNTs and SWNT-O_3 contain 0.7 at% and 2.5 at% oxygen, respectively, the Pt/SWNT and Pt/SWNT-O_3 samples contained 3.2 at% and 4.6 at% (Table 2). Deconvolution of the O 1*s* region was performed using five peaks. For transition metal oxides such as PtO/PtO_2 and Fe_2O_3, the O 1*s* peak is usually located around 530.2 eV, which is the value used here. [42,43] This peak contributes to only 4 % and 3 % of the total amount of oxygen in the Pt/SWNT and Pt/SWNT-O_3, meaning that most of the oxygen is present as oxygen functional groups and not Pt or Fe oxides. The three main oxygen peaks are identified as carbonyl C═O (531.4 eV), C−O groups such as hydroxyl and epoxide (532.2 eV) and O−C═O groups such as carboxyl and anhydride (533.3 eV). [29,30,44] Finally the peak at 534.7 eV is attributed to chemisorbed H_2O. [45] Especially the amount of C═O and O−C═O groups is higher for Pt/SWNT-O_3 compared to Pt/SWNT. These polar groups make the sample more hydrophilic, as indicated by goniometry (Figure S6), and they could also improve the catalyst wetting by ionomer, [46] and thereby improve the HER activity of Pt/SWNT-O_3 compared to Pt/SWNT.

3.5. Density functional theory calculations

To study the origin of the electrocatalytic activity, the structure and hydrogen adsorption properties of both a continuous PtNW and a truncated PtNW with exposed edge-sites on a SWNT were investigated using periodic density functional theory (DFT) calculations. As a reference, all calculations were repeated also on a close-packed Pt(111) surface. The reported simulations were performed using the CP2K/

Table 1
Best-fit parameters obtained from the EXAFS analysis of the bulk Pt, Pt/SWNT-O3 and Pt/SWNT. R (Å) is the interatomic distance, σ2 (10-3 Å2) is the Debye-Waller factor and N is the coordination number (for Pt foil the coordination numbers were fixed). Errors are given in parentheses.

Pt foil				Pt/SWNT-O_3			Pt/SWNT		
Shell	R	σ^2	*N*	R	σ^2	*N*	R	σ^2	*N*
I	2.776(2)	5.7(1)	12	2.769(2)	8.1(2)	11.8(2)	2.752(3)	11(1)	11.9(3)
II	3.920(5)	11(1)	6	3.918(9)	14(1)	4.8(8)	3.923(8)	15(1)	4.3(5)
III	4.808(3)	6.9(2)	24	4.795(5)	10(2)	22.2(8)	4.766(6)	19(1)	20.5(2.0)
IV	5.552(4)	11(1)	12	5.54(1)	18(1)	9(1)	5.50(1)	30(5)	9.5(1.0)

Table 2
Surface composition and distribution of the oxygen functional groups from the O 1s region by XPS analysis.

Sample	Pt [at%]	O [at%]	Fe [at%]	M_xO_y [%]	C = O [%]	C–O [%]	O–C = O [%]	H_2O [%]
SWNT	–	0.7	–	–	–	–	–	–
SWNT-O_3	–	2.9	0.07	7	27	36	24	6
Pt/SWNT	0.05	3.2	0.15	4	14	48	31	3
Pt/SWNT-O_3	0.11	4.6	0.12	3	19	41	33	4

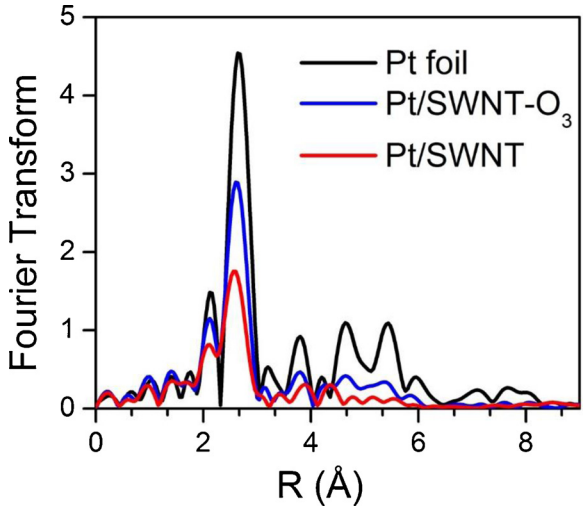

Fig. 7. Fourier transform of the experimental EXAFS spectra depicted in Fig. 6 for Pt foil, Pt/SWNT and Pt/SWNT-O3. Signals are calculated with no phase-shift correction applied.

Quickstep [47,48] quantum chemistry code at the RPBE/GGA [49] level of theory. A comprehensive description of the computational methodology is presented in the Supporting Information.

Based on the HAADF/STEM images shown in Fig. 2, both a periodic PtNW wrapped around a (10,0) SWNT and a truncated PtNW were constructed and their geometries were fully optimized with no applied constraints (Fig. 9). We refer to these model structures as Pt/SWNT and Pt/SWNT-O_3, considering that the ozone-treated system is proposed to contain shorter PtNWs and hence an increased edge-to-surface ratio. It is emphasized that the adopted naming convention refers exclusively to the experimental catalyst preparation methods and the resulting PtNW lengths, in contrast to explicit consideration of oxygen in the model systems. Although the experimental evidence of fully wrapped PtNWs is not complete, we argue that this structure is justified based on thermodynamic considerations and the highly regular hexagonal structure of the PtNW surfaces. Please see the Supporting Information for further discussion on the employed structural models. Furthermore, the advantage of the chosen angularly periodic model structures is that a complete decoupling of edge-effects from the intrinsic activity of the PtNW bulk surface is possible. Indeed, by deliberately excluding edge-sites along the angular axis, the properties of a fully edge-free and a truncated PtNW can be directly compared, enabling a more categorical analysis of the importance of edge-sites on the catalytic activity.

To assess the HER activity of the PtNWs, the hydrogen adsorption affinity of both model systems was systematically characterized using the method of atomistic thermodynamics introduced by Reuter and Scheffler [50] and later extended to the context of electrocatalysis by Nørskov et al. [51,52]. (see the Computational methods section in SI). First, the reactivities of the periodic and truncated Pt/SWNT systems were probed by studying the adsorption of a single hydrogen atom (low coverage limit) and calculating the associated change in free energy. As a reference, the calculations were repeated also for a pristine (10,0) SWNT and the Pt(111) surface. The obtained free energy diagram is presented in Fig. 10.

A qualitative prerequisite for a well-performing heterogeneous catalyst is that it should neither bind reaction intermediates too strongly nor too weakly. [53] In the case of HER, the hydrogen adsorption free energy of an efficient electrocatalyst should thus be close to 0 eV. Fig. 10 illustrates that the free energy of adsorption onto a bridge-site on the Pt/SWNT system is highly favorable, exhibiting a ΔG_H of ca. -0.31 eV. Truncating the periodic PtNW is observed to significantly alter the H adsorption properties of the system. Indeed, bridge-sites in the center of the truncated Pt/SWNT system are activated, demonstrating a ΔG_H of roughly -0.42 eV. On the other hand, hydrogen adsorption to bridge-sites on the PtNW edge is seen to weaken, resulting in a ΔG_H of -0.23 eV, which closely matches the corresponding values for Pt(111) fcc- and top-sites. As a reference, hydrogen adsorption onto a pristine SWNT is highly endergonic, ruling out the catalytic activity of the nanotube support as is also shown by the electrochemical experiments (Fig. 3a). In conclusion, hydrogen adsorption onto edge-sites on the PtNW appears to be energetically very similar to hydrogen adsorption on Pt(111) at the low coverage limit. Studying hydrogen adsorption at the low coverage limit provides insight into the intrinsic affinity of the material to bind hydrogen. However, it is crucial to additionally characterize the adsorption energetics as a function of the hydrogen coverage (θ) to evaluate the significance of lateral adsorbate-adsorbate interactions. Based on Fig. 10, all investigated Pt-containing systems demonstrate exergonic hydrogen adsorption, suggesting that the materials will continue to adsorb hydrogen until an eventual saturation coverage is reached. This assumes that there are repulsive interactions between the adsorbates, resulting in weaker adsorption as the coverage increases. At the saturation coverage, hydrogen atoms at the surface are in a dynamic equilibrium with both gaseous molecular hydrogen and protons in the electrolyte solution, thus indicating that the energetic prerequisite for efficient electrocatalysis is met. Hence, to systematically characterize the hydrogen adsorption energetics on the model systems, the formation energies and the differential adsorption free energies of various adsorbate-substrate configurations are estimated as a function of the hydrogen coverage. The obtained results are illustrated in Fig. 11 and have been calculated using the formalism outlined in the SI.

The formation energies presented in Fig. 11a reflect the change in energy per unit area due to a given hydrogen adsorption process resulting in a certain coverage θ. The formation energies on the Pt/SWNT models follow a very similar trend as a function of θ at sub-monolayer coverages. This can be explained by the fact that in both cases hydrogen adsorption occurs to bridge-sites in a similar local environment in the center of the PtNWs. However, at coverages above 1 ML, the exposed edge-sites on the truncated Pt/SWNT system start to adsorb hydrogen preferentially, thus enabling further decreased formation energies at the high coverage limit. On the periodic Pt/SWNT model, on the other hand, the repulsion between hydrogen adatoms becomes very substantial at high coverages, resulting in a rapidly increasing formation energy and thus destabilized surface structures. As a comparison, formation energies on the Pt(111) surface are consistently larger than for both PtNW models, indicative of their higher reactivity compared to bulk Pt.

Differentiating the formation energies in Fig. 11a with respect to the hydrogen coverage and applying appropriate finite-temperature corrections (Table S5) including configurational entropy yields the

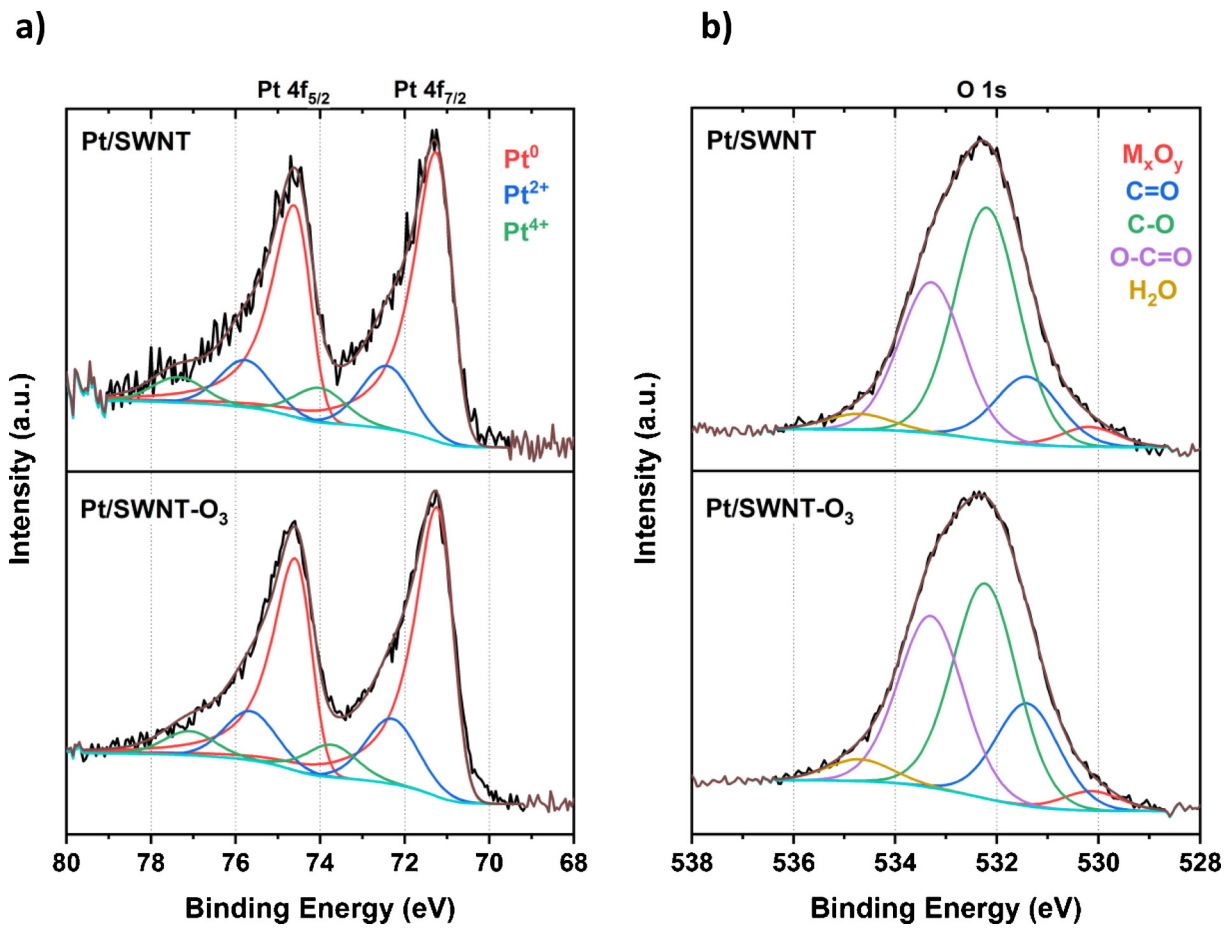

Fig. 8. High-resolution XPS spectra and deconvolution of the **a)** Pt 4f region and **b)** O 1s region for Pt/SWNT and Pt/SWNT-O_3.

differential free energy of hydrogen adsorption (Fig. 11b). For the Pt (111) reference system, the change in free energy due to hydrogen adsorption increases linearly in accordance with the Frumkin adsorption isotherm and the surface is observed to saturate at a coverage of roughly 0.7 ML, which is well in line with previous experimental estimates. [54] The adsorption free energy continues to increase linearly as the hydrogen coverage is incremented up until a full monolayer coverage, whereat all the preferential fcc hollow-sites are occupied. Adsorbing further hydrogen atoms to the next-most preferential top-sites results in a significant discontinuity in the differential adsorption free energy, which is also evidenced by the cusp in the corresponding formation energy plot in Fig. 11a. That this discontinuity occurs after the saturation coverage is reached supports the well-established fact that Pt (111) is a good HER catalyst. Indeed, if the adsorption free energy would exhibit an abrupt discontinuity at $\Delta G_H = 0$ eV the catalyst surface would always over- or underbind adsorbates and thus according to the applied thermodynamic model have a low catalytic activity. Such a behaviour is presumed to occur *e.g.* in the case of HER on single Pt atoms decorated on SWNTs and is experimentally evidenced by a gradual current decay in the cathodic potential region. [26]

According to Fig. 11b, the differential adsorption free energy on the periodic Pt/SWNT system is relatively constant at coverages below 0.8 ML, but past this point a very rapid increase in ΔG_H occurs such that the overall coverage dependence is well fitted by a parabolic function. The saturation coverage is roughly 1.1 ML, whereat the system is considered to fulfil the energetic prerequisite for HER activity. However, comparing with the truncated Pt/SWNT-O_3 model, a significantly weaker, linear coverage dependence that results in a higher equilibrium hydrogen coverage of 1.4 ML is observed. This difference is again attributed to the exposed edge-sites, which optimally adsorb hydrogen once all sites in the PtNW center become saturated, thereby avoiding increased repulsion between adsorbates.

The difference in adsorbate-adsorbate repulsion on the modelled PtNWs can be tentatively used to assess the experimentally observed variations in HER activity between the Pt/SWNT and the Pt/SWNT-O_3 catalysts. Indeed, the rapidly increasing adsorption free energy on the Pt/SWNT system significantly limits the coverage region in which HER catalysis may be considered efficient from a thermodynamic point of view. Furthermore, reactive species involved in the HER, namely solvated protons, must overcome a substantial interatomic repulsion as they approach the Pt/SWNT surface for the reaction to proceed. This has been previously proposed to also have and increasing effect on the associated activation barriers. [55] Also, considering the limiting case discussed in the previous paragraph, if an abrupt discontinuity in the adsorption free energy is observed precisely at the saturation coverage, a good catalytic activity is very likely to be lost. Although the increase for the continuous Pt/SWNT model appears to be continuous, it is nevertheless *ca.* one order of magnitude more rapid than what is observed for Pt(111) and truncated Pt/SWNT-O_3, which both exhibit approximately optimal $|\Delta G_H| < 0.1$ eV differential adsorption free energies in roughly 0.5 ML wide coverage windows.

Finally, to gain more insight into the electronic origin of the HER activity of the studied systems, the Pt 5*d* and H 1*s* projected density of states (PDOS) were calculated (Figure S18). The obtained PDOS reveal that both Pt/SWNT models demonstrate *d* -bands that span the Fermi level, indicative of a metallic character that corroborates the experimental results. Furthermore, employing the *d* -band theory of Hammer and Nørskov, [56,57] the obtained *d* -band centers of the investigated systems are found to correlate well with the preceding thermodynamic analysis, thus further supporting the notion of active PtNW edge-sites.

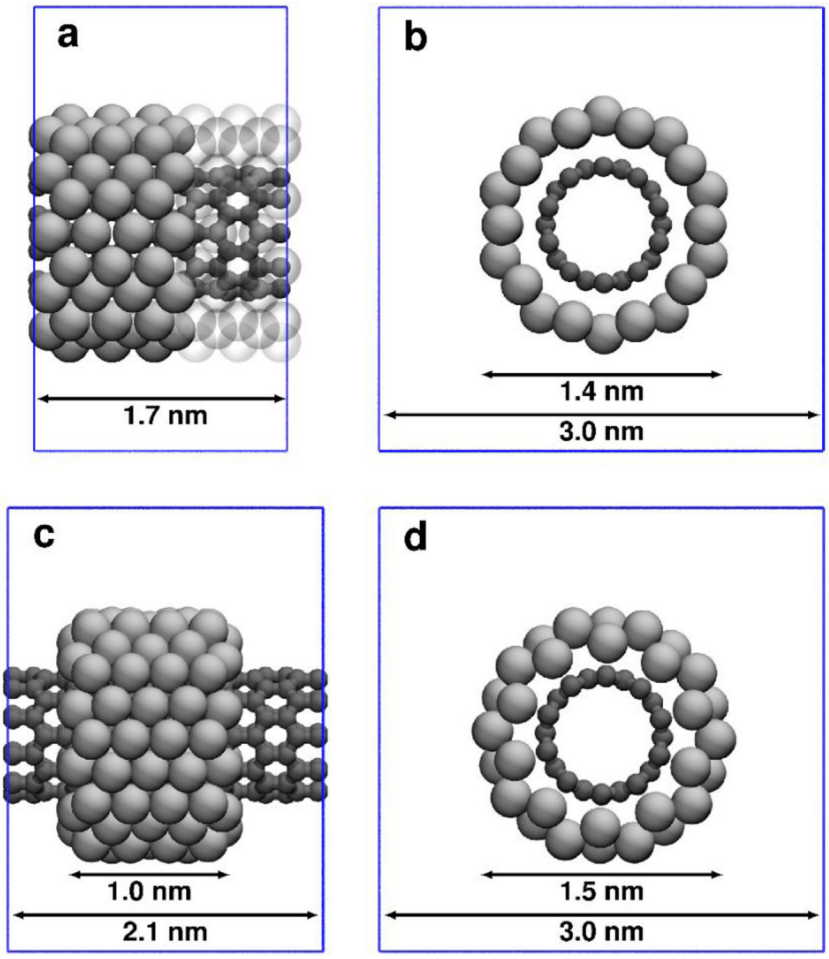

Fig. 9. Optimized structures of the periodic (a,b) and truncated (c,d) Pt/SWNT models viewed along the radial (a, c) and axial (b, d) directions. Dark gray and light gray spheres denote carbon and platinum atoms, respectively. To better visualize the underlying SWNT structure, a part of the Pt-atoms in (a) are shown as transparent. The blue rectangles mark the boundaries of the periodically repeated simulation cell. (For interpretation of the references to colour in this figure legend, the reader is referred to the web version of this article).

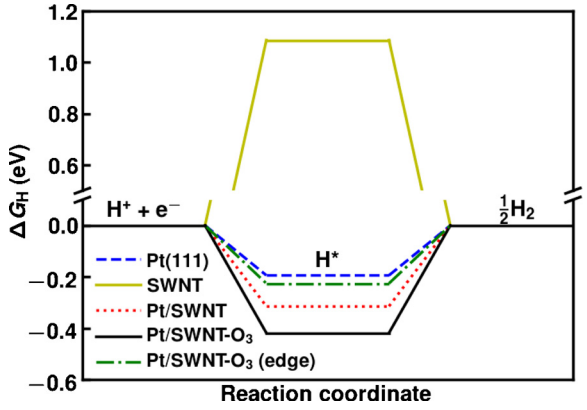

Fig. 10. Free energy diagram of the HER on preferential sites of the studied systems. In accordance with the computational hydrogen electrode (CHE) scheme, the initial and final states are assumed to be in a dynamic equilibrium. The probed adsorption sites are the fcc hollow-site on Pt(111), the atop C-site on the pristine (10,0) SWNT and various Pt-Pt bridge-sites on the PtNW systems.

4. Conclusions

We present a robust and upscalable three-step synthesis for preparing an unprecedented HER electrocatalyst with an ultralow Pt loading (340 ng cm^{-2}) on SWNTs. The ozone pre-treatment of the SWNTs results in shorter PtNWs and improved electrocatalytic efficiency compared with a non-ozonized counterpart. The high efficiency is attributed to a combined effect of better surface wetting and differences in the PtNW morphology.

In particular, the ozone treatment leads to an increased number of PtNW edge-sites with optimal hydrogen affinity. DFT calculations suggest that these edge-sites mitigate repulsions between hydrogen intermediaries on the PtNW at high coverages. Thus, the hydrogen coverage window within which the HER is thermodynamically feasible is broadened, and tentatively also the kinetic barrier is decreased. The proposed high activity of PtNW edges by the DFT calculations is in accordance with the experimental observations demonstrating higher mass activity of the sample containing shorter PtNWs on ozonized SWNTs than the non-ozonized Pt/SWNT catalyst. Furthermore, the ozone treatment also introduces polar surface groups on the nanotubes, turning the catalyst more hydrophilic than its non-ozonized counterpart and therefore more benign to hydrogen ions.

Our Pt/SWNT-O_3 catalyst outperforms a commercial Pt/C reference in the HER mass activity. In addition, Pt/SWNT-O_3 is proven feasible as the cathode catalyst of an electrolyzer, again approaching the activity and exceeding the stability of a commercial state-of-the-art reference, but with ten times less of precious Pt per electrode area. Because Pt/SWNT-O_3 can be prepared in a strikingly simple and upscalable manner, this work provides an interesting starting point for both manufacturing less costly PEM electrolyzers and for discovering other

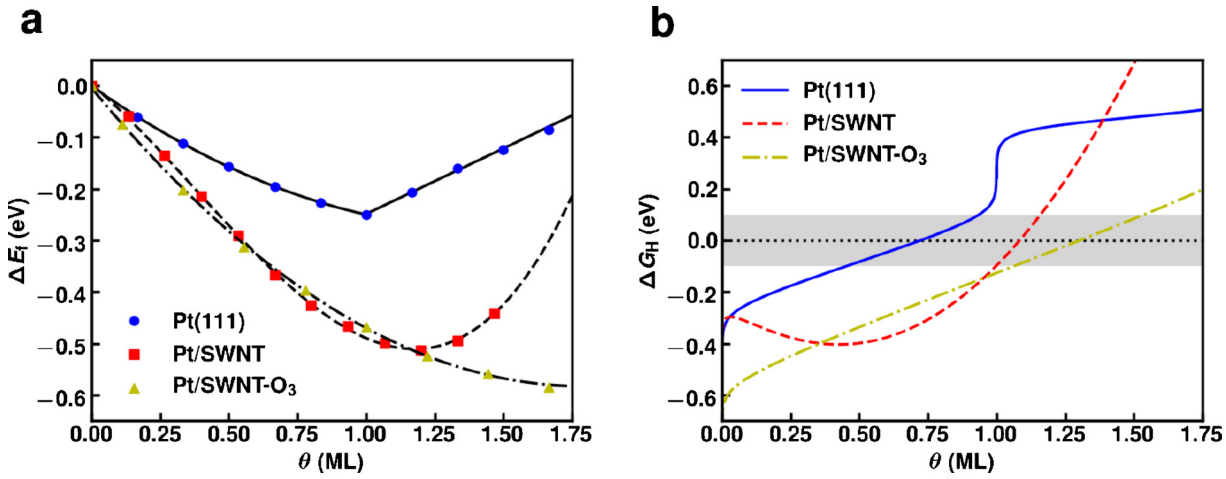

Fig. 11. Formation energy (a) and differential adsorption free energy (b) of hydrogen on the model PtNW systems and the Pt(111) reference. The results have been calculated according to the scheme presented in the Methods section. In (b), the shaded area highlights an adsorption energy interval [-0.1,0.1] eV where the energetic prerequisite for efficient HER catalysis is approximately met.

high-impact electrochemical reactions to catalyze.

Author contributions

T.R. carried out the electrochemical measurements under the supervision of T.K. and R.B. the electrolyzer tests. As for the imaging, M.T. carried out and interpreted HAADF/STEM under the supervision of T.S. and H.J. was responsible for the lower resolution STEM. M.E.M.B. carried out and interpreted XPS and A. Z. XAS/EXAFS. R.K. did the computational studies under the supervision of K.L. F.J. contributed to planning of the electrochemical characterization. The idea was conveyed and developed by T.R. and T.K. All the authors contributed to data interpretation and writing of the manuscript. T.K. supervised the work.

Declaration of Competing Interest

The authors declare no competing interests.

Acknowledgements

The research leading to these results has received funding from the European Union's Horizon 2020 research and innovation programme under grant agreement CREATE No. 721065. In addition, Academy of Finland (Profi 5) is greatly acknowledged for the financial support. M.T. and T.S. acknowledge the financial support of the Austrian Science Fund (FWF) via project P 28322-N36. The authors also thank Marton Helén from the Energy Platform at Aalto University for creating some of the visualizations featured in this article. Moreover, Mr. Florian Speck and Ms. Andrea Mingers are acknowledged for the ICP-MS results, Olli Sorsa for the Raman study and Mr. Paulus Saari for the goniometric results. This study used OtaNano and RaM infrastructures.

Appendix A. Supplementary data

Supplementary material related to this article can be found, in the online version, at doi:https://doi.org/10.1016/j.apcatb.2019.118582.

References

[1] V. PS, M.R. Nouni, S. Jain, S. Goel, J.K. Pandey, S. Singh, A.K. Tiwari, Hydrogen: A sustainable fuel for future of the transport sector, Renew. Sustain. Energy Rev. 51 (2015) 623–633, https://doi.org/10.1016/j.rser.2015.06.040.
[2] Y. Tachibana, L. Vayssieres, J.R. Durrant, Artificial photosynthesis for solar water-splitting, Nat. Photonics 6 (2012) 511–518, https://doi.org/10.1038/nphoton.2012.175.
[3] N.S. Lewis, D.G. Nocera, Powering the planet: chemical challenges in solar energy utilization, Proc. Natl. Acad. Sci. 103 (2006) 15729–15735, https://doi.org/10.1073/pnas.0603395103.
[4] N. Armaroli, V. Balzani, The hydrogen issue, ChemSusChem (2011) 21–36, https://doi.org/10.1002/cssc.201000182.
[5] F. Barbir, PEM electrolysis for production of hydrogen from renewable energy sources, Sol. Energy 78 (2005) 661–669, https://doi.org/10.1016/j.solener.2004.09.003.
[6] H. Du, R. Kong, X. Guo, F. Qu, J. Li, Recent progress in transition metal phosphides with enhanced electrocatalysis for hydrogen evolution, Nanoscale (2018) 21617–21624, https://doi.org/10.1039/c8nr07891b.
[7] X. Wang, Y.V. Kolen, X. Bao, K. Kovnir, L. Liu, Angewandte One-Step Synthesis of Self-Supported Nickel Phosphide Nanosheet Array Cathodes for Efficient Electrocatalytic Hydrogen Generation **, (2015), pp. 8188–8192, https://doi.org/10.1002/anie.201502577.
[8] S. Jing, L. Zhang, L. Luo, J. Lu, S. Yin, P. Kang, Environmental N-Doped porous molybdenum carbide nanobelts as efficient catalysts for hydrogen evolution reaction, Appl. Catal. B Environ. 224 (2018) 533–540, https://doi.org/10.1016/j.apcatb.2017.10.025.
[9] J. Wang, W. Chen, T. Wang, N. Bate, C. Wang, E. Wang, A strategy for highly dispersed Mo2C/MoN hybrid nitrogen-doped graphene via ion-exchange resin synthesis for efficient electrocatalytic hydrogen reduction, Nano Res. 11 (2018) 4535–4548.
[10] Y. Zhong, X. Xia, F. Shi, J. Zhan, J. Tu, H.J. Fan, Transition metal carbides and nitrides in energy storage and conversion, Adv. Sci. 3 (2016), https://doi.org/10.1002/advs.201500286.
[11] D.R. Cummins, U. Martinez, A. Sherehiy, R. Kappera, A. Martinez-garcia, R.K. Schulze, J. Jasinski, J. Zhang, R.K. Gupta, J. Lou, M. Chhowalla, G. Sumanasekera, A.D. Mohite, M.K. Sunkara, G. Gupta, Efficient hydrogen evolution in transition metal dichalcogenides via a simple one-step hydrazine reaction, Nat. Commun. 7 (2016) 1–10, https://doi.org/10.1038/ncomms11857.
[12] D. Escalera-lo, Y. Niu, J. Yin, K. Cooke, N.V. Rees, R.E. Palmer, Enhancement of the hydrogen evolution reaction from Ni-MoS 2, Hybrid Nanoclusters (2016) 6008–6017, https://doi.org/10.1021/acscatal.6b01274.
[13] P. Wang, X. Zhang, J. Zhang, S. Wan, S. Guo, G. Lu, J. Yao, X. Huang, Precise tuning in platinum-nickel/nickel sulfide interface nanowires for synergistic hydrogen evolution catalysis, Nat. Commun. 8 (2017) 1–9, https://doi.org/10.1038/ncomms14580.
[14] L. Fan, P.F. Liu, X. Yan, L. Gu, Z.Z. Yang, H.G. Yang, S. Qiu, X. Yao, Atomically isolated nickel species anchored on graphitized carbon for efficient hydrogen evolution electrocatalysis, Nat. Commun. 7 (2016) 1–7, https://doi.org/10.1038/ncomms10667.
[15] M. Zeng, Y. Li, Recent advances in heterogeneous electrocatalysts, J. Mater. Chem. A Mater. Energy Sustain. (2015) 14942–14962, https://doi.org/10.1039/c5ta02974k.
[16] E. Brightman, J. Dodwell, N. Van Dijk, G. Hinds, In situ characterisation of PEM water electrolysers using a novel reference electrode, Electrochem. commun. 52 (2015) 1–4, https://doi.org/10.1016/j.elecom.2015.01.005.
[17] H. Zhao, D. Wang, C. Gao, H. Liu, L. Han, Y. Yin, Ultrafine platinum/iron oxide nanoconjugates confined in silica nanoshells for highly durable catalytic oxidation, J. Mater. Chem. A Mater. Energy Sustain. 4 (2016) 1366–1372, https://doi.org/10.1039/C5TA09215A.
[18] Y. Zhai, D. Pierre, R. Si, W. Deng, P. Ferrin, A.U. Nilekar, G. Peng, J.A. Herron, D.C. Bell, H. Saltsburg, M. Mavrikakis, M. Flytzani-Stephanopoulos, Alkali-stabilized Pt-OHx species catalyze low-temperature water-gas shift reactions, Science 329 (2010) 1633–1636, https://doi.org/10.1126/science.1192449.
[19] B. Qiao, A. Wang, X. Yang, L.F. Allard, Z. Jiang, Y. Cui, J. Liu, J. Li, T. Zhang, Single-

atom catalysis of CO oxidation using Pt1/FeOx, Nat. Chem. 3 (2011) 634–641, https://doi.org/10.1038/nchem.1095.
[20] M. Moses-Debusk, M. Yoon, L.F. Allard, D.R. Mullins, Z. Wu, X. Yang, G. Veith, G.M. Stocks, C.K. Narula, CO oxidation on supported single Pt atoms: experimental and ab initio density functional studies of CO interaction with Pt atom on θ-Al2O3(010) surface, J. Am. Chem. Soc. 135 (2013) 12634–12645, https://doi.org/10.1021/ja401847c.
[21] F. Dvořák, M.F. Camellone, A. Tovt, N.D. Tran, F.R. Negreiros, M. Vorokhta, T. Skála, I. Matolínová, J. Mysliveček, V. Matolín, S. Fabris, Creating single-atom Pt-ceria catalysts by surface step decoration, Nat. Commun. 7 (2016), https://doi.org/10.1038/ncomms10801.
[22] A. Bruix, Y. Lykhach, I. Matolínová, A. Neitzel, T. Skála, N. Tsud, M. Vorokhta, V. Stetsovych, K. Ševčíková, J. Mysliveček, R. Fiala, M. Václavu, K.C. Prince, S. Bruyère, V. Potin, F. Illas, V. Matolín, J. Libuda, K.M. Neyman, Maximum noble-metal efficiency in catalytic materials: atomically dispersed surface platinum, Angew. Chemie 53 (2014) 10525–10530, https://doi.org/10.1002/anie.201402342.
[23] N. Cheng, S. Stambula, D. Wang, M.N. Banis, J. Liu, A. Riese, B. Xiao, R. Li, T.K. Sham, L.M. Liu, G.A. Botton, X. Sun, Platinum single-atom and cluster catalysis of the hydrogen evolution reaction, Nat. Commun. 7 (2016) 1–9, https://doi.org/10.1038/ncomms13638.
[24] S.T. Hunt, M. Milina, Z. Wang, Y. Roma, Activating eart-abundant electrocatalysts for efficient, low-cost hydrogen evolution/oxidation: sub-monolayer platinum coatings on titanium tungsten carbide nanoparticles, Energy Environ. Sci. (2016) 3290–3301, https://doi.org/10.1039/c6ee01929c.
[25] D. Liu, X. Li, S. Chen, H. Yan, C. Wang, C. Wu, Y.A. Haleem, S. Duan, J. Lu, B. Ge, P.M. Ajayan, Y. Luo, Electrocatalytic hydrogen evolution, Nat. Energy. 4 (2019) 3–9, https://doi.org/10.1038/s41560-019-0402-6.
[26] M. Tavakkoli, N. Holmberg, R. Kronberg, H. Jiang, J. Sainio, E.I. Kauppinen, T. Kallio, K. Laasonen, Electrochemical activation of single-walled carbon nanotubes with pseudo-atomic-Scale platinum for the hydrogen evolution reaction, ACS Catal. 7 (2017) 3121–3130, https://doi.org/10.1021/acscatal.7b00199.
[27] G. Wu, B. Xu, Carbon nanotube supported Pt electrodes for methanol oxidation: a comparison between multi- and single-walled carbon nanotubes, J. Power Sources 174 (2007) 148–158, https://doi.org/10.1016/j.jpowsour.2007.08.024.
[28] P.P. Pal, T. Larionova, I.V. Anoshkin, H. Jiang, M. Nisula, A.A. Goryunkov, O.V. Tolochko, M. Karppinen, E.I. Kauppinen, A.G. Nasibulin, Dry functionalization and doping of single-walled carbon nanotubes by ozone, J. Phys. Chem. C. 119 (2015) 27821–27828, https://doi.org/10.1021/acs.jpcc.5b08832.
[29] P. Cañete-Rosales, V. Ortega, A. Álvarez-Lueje, S. Bollo, M. González, A. Ansón, M.T. Martínez, Influence of size and oxidative treatments of multi-walled carbon nanotubes on their electrocatalytic properties, Electrochim. Acta 62 (2012) 163–171, https://doi.org/10.1016/j.electacta.2011.12.043.
[30] U. Zielke, K.J. Hüttinger, W.P. Hoffman, Surface-oxidized carbon fibers: I. Surface structure and chemistry, Carbon 34 (1996) 983–998, https://doi.org/10.1016/0008-6223(96)00032-2.
[31] A. Govindaraj, B.C. Satishkumar, M. Nath, C.N.R. Rao, Metal Nanowires, Intercalated metal layers in single-walled carbon nanotube bundles, Chem. Mater. 12 (2000) 202–205, https://doi.org/10.1021/CM990546O.
[32] M. Lin, M. Lo, C. Mou, PtRu Nanoparticles Supported on Ozone-Treated Mesoporous Carbon Thin Film As Highly Active Anode Materials for Direct Methanol Fuel Cells, (2009), pp. 16158–16168.
[33] A. Battistel, C.R. Dennison, A. Lesch, H.H. Girault, Local study on hydrogen and hydrogen gas bubble formation on a platinum electrode, J. Phys. Chem. C. 123 (2019) 10849–10856, https://doi.org/10.1021/acs.jpcc.8b10920.
[34] F.S. Fedorov, M.Y. Vasilkov, M. Panov, D. Rupasov, A. Rashkovskiy, N.M. Ushakov, J. Lee, R. Hempelmann, T. Kallio, A.G. Nasibulin, ScienceDirect Tailoring electrochemical efficiency of hydrogen evolution by fine tuning of TiO x / RuO x composite cathode architecture, Int. J. Hydrogen Energy 44 (2019) 10593–10603, https://doi.org/10.1016/j.ijhydene.2019.03.019.
[35] Z. Lu, W. Zhu, X. Yu, H. Zhang, Y. Li, X. Sun, X. Wang, H. Wang, J. Wang, J. Luo, X. Lei, L. Jiang, Ultrahigh hydrogen evolution performance of under-water "Superaerophobic" MoS2 nanostructured electrodes, Adv. Mat. (2014) 2683–2687, https://doi.org/10.1002/adma.201304759.
[36] W. Xu, Z. Lu, X. Sun, L. Jiang, X. Duan, Superwetting electrodes for gas-involving electrocatalysis, Acc. Chem. Res. 51 (2018) 1590–1598, https://doi.org/10.1021/acs.accounts.8b00070.
[37] E. Brightman, J. Dodwell, N. Van Dijk, G. Hinds, Electrochemistry Communications in situ characterisation of PEM water electrolysers using a novel reference electrode, Electrochem. commun. 52 (2015) 1–4, https://doi.org/10.1016/j.elecom.2015.01.005.
[38] R.W.G. Wyckoff, Cryst. Struct. 1 (2) (1963) 7–83.
[39] J. Woltersdorf, A.S. Nepijko, E. Pippel, Dependence of lattice parameters of small particles on the size of the nuclei, Surf. Sci. 106 (1981) 64–69, https://doi.org/10.1016/0039-6028(81)90182-5.
[40] M. Luo, S. Guo, Strain-controlled electrocatalysis on multimetallic nanomaterials, Nat. Rev. Mater. 2 (2017) 17059, https://doi.org/10.1038/natrevmats.2017.59.
[41] L.K. Ono, B. Yuan, H. Heinrich, B. Roldan Cuenya, Formation and thermal stability of platinum oxides on size-selected platinum nanoparticles: support effects, J. Phys. Chem. C. 114 (2010) 22119–22133, https://doi.org/10.1021/jp1086703.
[42] D.A. Svintsitskiy, L.S. Kibis, A.I. Stadnichenko, S.V. Koscheev, V.I. Zaikovskii, A.I. Boronin, Highly oxidized platinum nanoparticles prepared through radio-frequency sputtering: thermal stability and reaction probability towards CO, ChemPhysChem. 16 (2015) 3318–3324, https://doi.org/10.1002/cphc.201500546.
[43] M.C. Biesinger, B.P. Payne, A.P. Grosvenor, L.W.M. Lau, A.R. Gerson, R.S.C. Smart, Resolving surface chemical states in XPS analysis of first row transition metals, oxides and hydroxides: Cr, Mn, Fe, Co and Ni, Appl. Surf. Sci. 257 (2011) 2717–2730, https://doi.org/10.1016/J.APSUSC.2010.10.051.
[44] L. Stobinski, B. Lesiak, A. Malolepszy, M. Mazurkiewicz, B. Mierzwa, J. Zemek, P. Jiricek, I. Bieloshapka, Graphene oxide and reduced graphene oxide studied by the XRD, TEM and electron spectroscopy methods, J. Electron Spectros. Relat. Phenomena 195 (2014) 145–154, https://doi.org/10.1016/j.elspec.2014.07.003.
[45] F. Vautard, H. Grappe, S. Ozcan, Stability of carbon fiber surface functionality at elevated temperatures and its influence on interfacial adhesion, Appl. Surf. Sci. 268 (2013) 61–72, https://doi.org/10.1016/j.apsusc.2012.11.158.
[46] K. Artyushkova, M.J. Workman, S. Pylypenko, I. Matanovic, P. Atanassov, A. Serov, C. Ngo, M.J. Dzara, Role of surface chemistry on Catalyst/Ionomer interactions for transition metal–nitrogen–carbon electrocatalysts, ACS Appl. Energy Mater. 1 (2017) 68–77, https://doi.org/10.1021/acsaem.7b00002.
[47] J. Vandevondele, M. Krack, F. Mohamed, M. Parrinello, T. Chassaing, J. Hutter, Quickstep: Fast and accurate density functional calculations using a mixed Gaussian and plane waves approach, Comput. Phys. Commun. 167 (2005) 103–128, https://doi.org/10.1016/j.cpc.2004.12.014.
[48] J. Hutter, M. Iannuzzi, F. Schiffmann, J. Vandevondele, Cp2k: Atomistic simulations of condensed matter systems, Wiley Interdiscip. Rev. Comput. Mol. Sci. 4 (2014) 15–25, https://doi.org/10.1002/wcms.1159.
[49] B. Hammer, L.B. Hansen, J.K. Nørskov, Improved adsorption energetics within density-functional theory using revised Perdew-Burke-Ernzerhof functionals, Phys. Rev. B - Condens. Matter Mater. Phys. 59 (1999) 7413–7421, https://doi.org/10.1103/PhysRevB.59.7413.
[50] K. Reuter, M. Scheffler, Composition, structure, and stability of RuO2(110) as a function of oxygen pressure, Phys. Rev. B - Condens. Matter Mater. Phys. 65 (2001) 035406, , https://doi.org/10.1103/PhysRevB.65.035406.
[51] J.K. Nørskov, J. Rossmeisl, A. Logadottir, L. Lindqvist, J.R. Kitchin, T. Bligaard, H. Jónsson, Origin of the overpotential for oxygen reduction at a fuel-cell cathode, J. Phys. Chem. B 108 (2004) 17886–17892, https://doi.org/10.1021/jp047349j.
[52] J.K. Nørskov, T. Bligaard, A. Logadottir, J.R. Kitchin, J.G. Chen, S. Pandelov, U. Stimming, Trends in the exchange current for hydrogen evolution, J. Electrochem. Soc. 152 (2005) J23, https://doi.org/10.1149/1.1856988.
[53] M.T.M. Koper, E. Bouwman, Electrochemical hydrogen production: bridging homogeneous and heterogeneous catalysis, Angew. Chem. 49 (2010) 3723–3725, https://doi.org/10.1002/anie.201000629.
[54] N.M. Marković, B.N. Grgur, P.N. Ross, Temperature-dependent hydrogen electrochemistry on platinum low-index single-crystal surfaces in acid solutions, J. Phys. Chem. B 101 (1997) 5405–5413, https://doi.org/10.1139/v97-176.
[55] G. Soldano, E.N. Schulz, D.R. Salinas, E. Santos, W. Schmickler, Hydrogen electrocatalysis on overlayers of rhodium over gold and palladium substrates - More active than platinum? Phys. Chem. Chem. Phys. 13 (2011) 16437–16443, https://doi.org/10.1039/c1cp21565e.
[56] B. Hammer, J.K. Nørskov, Electronic factors determining the reactivity of metal surfaces, Surf. Sci. 343 (1995) 211–220, https://doi.org/10.1016/0039-6028(96)80007-0.
[57] B. Hammer, J.K. Norskov, Why gold is the noblest of all the metals, Nature 376 (1995) 238–240, https://doi.org/10.1038/376238a0.